The Astrophysical Journal, 707:1740–1749, 2009 December 20 doi:10.1088/0004-637X/707/2/1740


# BLAST: A FAR-INFRARED MEASUREMENT OF THE HISTORY OF STAR FORMATION

Enzo Pascale[1], Peter A. R. Ade[1], James J. Bock[2], Edward L. Chapin[3], Mark J. Devlin[4], Simon Dye[1], Steve A. Eales[1], Matthew Griffin[1], Joshua O. Gundersen[5], Mark Halpern[3], Peter C. Hargrave[1], David H. Hughes[6], Jeff Klein[4], Gaelen Marsden[3], Philip Mauskopf[1], Lorenzo Moncelsi[1], Henry Ngo[3], Calvin B. Netterfield[7,8], Luca Olmi[9,10], Guillaume Patanchon[11], Marie Rex[4], Douglas Scott[3], Christopher Semisch[4], Nicholas Thomas[5], Matthew D. P. Truch[4], Carole Tucker[1], Gregory S. Tucker[12], Marco P. Viero[8], and Donald V. Wiebe[3,8]

[1] School of Physics & Astronomy, Cardiff University, 5 The Parade, Cardiff, CF24 3AA, UK; enzo.pascale@astro.cf.ac.uk
[2] Jet Propulsion Laboratory, Pasadena, CA 91109-8099, USA
[3] Department of Physics & Astronomy, University of British Columbia, 6224 Agricultural Road, Vancouver, BC V6T 1Z1, Canada
[4] Department of Physics & Astronomy, University of Pennsylvania, 209 South 33rd Street, Philadelphia, PA, 19104, USA
[5] Department of Physics, University of Miami, 1320 Campo Sano Drive, Coral Gables, FL 33146, USA
[6] Instituto Nacional de Astrofísica Óptica y Electrónica (INAOE), Aptdo. Postal 51 y 72000 Puebla, Mexico
[7] Department of Astronomy & Astrophysics, University of Toronto, 50 St. George Street Toronto, ON M5S 3H4, Canada
[8] Department of Physics, University of Toronto, 60 St. George Street, Toronto, ON M5S 1A7, Canada
[9] University of Puerto Rico, Rio Piedras Campus, Physics Department, Box 23343, UPR station, PR 00931, USA
[10] INAF, Osservatorio Astrofisico di Arcetri, Largo E. Fermi 5, I-50125, Firenze, Italy
[11] Université Paris Diderot, Laboratoire APC, 10, rue Alice Domon et Léonie Duquet 75205 Paris, France
[12] Department of Physics, Brown University, 182 Hope Street, Providence, RI 02912, USA
*Received 2009 April 8; accepted 2009 September 30; published 2009 December 7*

## ABSTRACT

We directly measure redshift evolution in the mean physical properties (far-infrared luminosity, temperature, and mass) of the galaxies that produce the cosmic infrared background (CIB), using measurements from the Balloon-borne Large Aperture Submillimeter Telescope (BLAST), and *Spitzer* which constrain the CIB emission peak. This sample is known to produce a surface brightness in the BLAST bands consistent with the full CIB, and photometric redshifts are identified for all of the objects. We find that most of the 70 $\mu$m background is generated at $z \lesssim 1$ and the 500 $\mu$m background generated at $z \gtrsim 1$. A significant growth is observed in the mean luminosity from $\sim 10^9$–$10^{12}$ $L_\odot$, and in the mean temperature by 10 K, from redshifts $0 < z < 3$. However, there is only weak positive evolution in the comoving dust mass in these galaxies across the same redshift range. We also measure the evolution of the far-infrared luminosity density, and the star formation rate history for these objects, finding good agreement with other infrared studies up to $z \sim 1$, exceeding the contribution attributed to optically selected galaxies.

*Key words:* cosmology: observations – diffuse radiation – galaxies: evolution – galaxies: starburst – submillimeter

## 1. INTRODUCTION

The spectrum of the diffuse extragalactic background radiation reflects the physical processes that have dominated the evolution of structure in the universe. The cosmic microwave background (CMB), the relic radiation of the early universe, is the dominant contribution.

The second most important component consists of two broad peaks at around 200 $\mu$m and 1 $\mu$m, which carry roughly equal energy and are presumably associated with light emitted by stars throughout cosmic time. In the far-infrared (FIR), the isotropic cosmic infrared background (CIB) was first detected with the FIRAS (Puget et al. 1996; Fixsen et al. 1998) and DIRBE (Hauser et al. 1998) instruments on board the *COBE* satellite. It consists of thermal emission from warm dust which enshrouds star-forming regions in galaxies; thus, a detailed account of the CIB will, by necessity, include constraints on the history of star formation in the universe (see also Dwek et al. 1998; Hauser & Dwek 2001). In strong contrast to the emission at $\approx 1$ $\mu$m, the warm dust is optically thin, so its intensity reveals the entire mass without assumptions or corrections. In this paper, we resolve the contribution to the CIB as a function of redshift. This constitutes a measurement of the FIR history of the universe that is closely related to the history of star and galaxy formation.

Large fractions of the CIB have been resolved into contributions from individual sources at 24 $\mu$m, 850 $\mu$m, and 1.1 mm (Lagache et al. 2005, and references therein), but the background is several tens of times smaller at these wavelengths than it is at its peak. Near the peak, current and anticipated FIR and submillimeter experiments, including the SPIRE instrument (Griffin et al. 2003) on the *Herschel* satellite, cannot resolve the CIB into individually detected sources because of confusion arising from the finite instrumental angular resolution.

It is, however, possible to study the *average* contribution that a given class of objects makes to the background with a stacking analysis consisting of calculating the covariance of known source positions with maps from these experiments. This approach has been successfully used by many authors (e.g., Dole et al. 2006; Dye et al. 2007; Serjeant et al. 2008). Individual sources brighter than 60 $\mu$Jy detected in deep surveys with the Multiband Imaging Photometer for *Spitzer* (MIPS) at 24 $\mu$m resolve most of the CIB at 24 $\mu$m ($\sim$70%; Papovich et al. 2004). Stacking analyses have shown that MIPS sources constitute a large fraction of the background at 70 and 160 $\mu$m ($\sim$ 80%; Dole et al. 2006). The bulk of this emission is from comparatively low redshift galaxies, while at 850 $\mu$m and 1 mm, the CIB is dominated by massive star-forming galaxies at higher redshifts ($z \approx 2.5$). Besides, Dye et al. (2007) determine that these extreme galaxies contribute relatively little emission to the important region near the CIB peak, which forms the transition between plentiful nearby galaxies and rarer distant sources of the submillimeter regime.

Balloon-borne Large Aperture Submillimeter Telescope (BLAST) has observed an 8.7 deg$^2$ region encompassing the

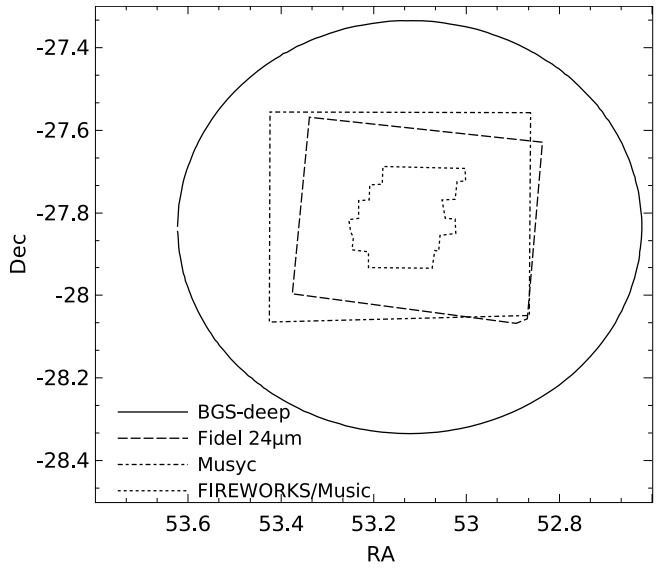


**Figure 1.** Extent of the catalogs in the BGS-Deep region observed with BLAST. The area used for the stacking analysis is the intersection of the FIDEL and MUSYC regions and extends over 590 arcmin$^2$.

Extended Chandra Deep Field South (ECDFS) and Great Observatories Origins Deep Survey South (GOODS-S). Additional time was spent observing a smaller 0.9 deg$^2$ area at the center of this field, though the coverage is still broader than most of the other deep data available at other wavelengths. We refer to these fields as BLAST GOODS-S Wide (BGS-Wide) and BLAST GOODS-S Deep (BGS-Deep), respectively. We note that the variance of the BGS-Deep maps are dominated by the confusion from point sources arising from the 36″–60″ BLAST beams, rather than instrumental noise.

Observing in three broad bands centered at 250, 350, and 500 $\mu$m, BLAST provides a new data set of unique size, resolution, and spectral coverage to study the properties of the CIB on the submillimeter side of its maximum. Together with MIPS observations at 70 $\mu$m, it is now possible to constrain the CIB without assumptions about any of the physical properties of the sources contributing to it.

The possibility of determining number counts, spectral energy distributions (SEDs), and clustering properties of submillimeter sources directly from correlations *within* the maps, without the requirement to first extract a catalog of point sources, was pointed out by Knox et al. (2001). The approach has the important advantage of avoiding flux and number density biases associated with the process of catalog selection. Devlin et al. (2009) and Patanchon et al. (2009) use this approach to estimate the number counts of extragalactic sources in the BLAST bands across nearly 5 orders of magnitude in flux density; and Viero et al. (2009) measure the clustering of BLAST sources via the power spectrum.

Devlin et al. (2009), Marsden et al. (2009), and this work extend that idea by measuring the covariance with external data sets, but again without forming a BLAST catalog, which is instead studied by Dye et al. (2009) who find MIR and radio counterparts for a sample of bright BLAST sources and measure their redshift distribution. Using this stacking technique, it is found that the total intensity emitted by MIPS 24 $\mu$m-selected sources at the BLAST wavelengths is compatible with the FIRAS measurements of the CIB intensity within the FIRAS 1$\sigma$ uncertainty, which is $\approx$ 25%. The 24 $\mu$m-selected source redshift distribution has a median of $z \approx 0.9$ (see Section 3); and it is certainly possible that a population with fainter 24 $\mu$m flux densities is missing, possibly associated with the submillimeter galaxies detected by SCUBA and MAMBO.

We extend this work by finding the covariance with catalogs which contain redshift information. We present a detailed analysis of all sources that contribute significantly to the CIB at 70 $\mu$m, 250 $\mu$m, 350 $\mu$m, and 500 $\mu$m as a function of redshift, even those well below the confusion limit. From this, we derive the evolutionary history of the CIB. The results from these five analysis papers will be used by E. L. Chapin et al. (2010, in preparation) to infer the evolution of the FIR luminosity function.

A portion of the BGS-Deep region has been surveyed at many wavelengths from which we have derived an almost complete set of redshifts ($\sim$ 95%) for MIPS sources. By exploiting BLAST and MIPS 70 $\mu$m data, we estimate the mean physical parameters for these galaxies (FIR luminosities, temperatures, and dust masses), and the total FIR luminosity evolution and star formation history of the universe. Our results are in good agreement with existing measurements. We find that stars form in optically obscured dusty galaxies at rates $\sim$ 3 times larger than those previously estimated from optical data at redshifts up to $z \sim 1$. We also estimate the variation of the total comoving dust mass density with redshift, finding only moderate evolution, within the experimental uncertainties, over the range $z \lesssim 3$.

A flat cosmological model with $\Omega_\Lambda = 0.7$ and $h = 0.7$ has been used throughout.

## 2. DATA

In this section, we describe each of the data sets used. Their locations and angular extents are depicted in Figure 1.

### *2.1. BLAST Submillimeter Imaging*

The BGS-Deep region observed with BLAST covers the central 0.9 deg$^2$ of a shallower map imaging the full 8.7 deg$^2$ area in BGS-Wide.

The raw time ordered data (TOD), consisting of a set of voltage time-streams from each of the BLAST detectors, are pre-processed (Truch et al. 2008; Patanchon et al. 2008). Any corrupt samples are flagged, and the data are deconvolved using the instrumental transfer functions. The TODs are binned into maps using the telescope pointing solution (Pascale et al. 2008), which has an estimated rms positional error of less than 5″ (Marsden et al. 2008). The absolute photometric calibration has an estimated accuracy of $\sim$10%, which is highly correlated across the BLAST bands (Truch et al. 2009). Calibration errors and color corrections are accounted for in our SED fits.

The maps used in this work have been generated using OPTBIN (E. Pascale et al. 2010, in preparation). The algorithm performs common-mode suppression and high-pass filters the output above the low-frequency "knee" of the detector noise. The filtered data streams are then projected onto a map. This treatment is appropriate for point-source extraction as it does not distort the data on timescales comparable to the beam-crossing times. OPTBIN reduces the 100 hr long BGS-Wide data set at 250 $\mu$m in 1 hr on a single-CPU machine, and it is also used as part of an end-to-end instrumental simulator which allows Monte Carlo analysis.

Results have been compared and found to be compatible with those obtained using maps reduced with the more computationally intensive SANEPIC algorithm (Patanchon et al. 2008), which provides the least-squares solution to the map-making equation.

### 2.2. Spitzer Data

Extensive *Spitzer* maps cover most of the BGS-Deep and -Wide regions. The *Spitzer* Wide-Area Infrared Extragalactic survey (SWIRE; Lonsdale et al. 2003, data release 3), provides ∼7.5 deg$^2$ maps well matched to the BGS-Wide coverage. We use the BLAST data in conjunction with the 70 $\mu$m SWIRE data to constrain the brightness of the peak in the CIB.

Deep imaging of this field is available in the four Infrared Array Camera (IRAC) bands from the SIMPLE (*Spitzer*'s IRAC and MUSYC Public Legacy of the ECDFS; Damen et al. 2009) survey. MIPS data from the *Spitzer* Far-Infrared Deep Extragalactic Legacy (FIDEL) survey are also available. The catalog of 24 $\mu$m sources detected in the FIDEL maps of Magnelli et al. (2009) is the same as used by Devlin et al. (2009) and Marsden et al. (2009), and utilizes the IRAC sources detected in SIMPLE as a positional prior.

The faintest 24 $\mu$m source in the catalog has a flux density of 13 $\mu$Jy, but the detections at $S_{24} < 30\,\mu$Jy should be considered tentative. The catalog includes 9110 sources covering 700 arcmin$^2$, with IRAC flux densities (at 3.6, 4.5, 5.8, and 8 $\mu$m) available for each entry.

### 2.3. Optical Photometric Redshifts

We use five different catalogs of photometric redshifts available in the BGS-Deep region to assign a redshift to the majority of the MIR sources in the FIDEL catalog.

Brammer et al. (2008) released two catalogs of photometric redshifts in the BGS-Deep region using Multiwavelength Survey by Yale-Chile (MUSYC; Taylor et al. 2009) and FIREWORKS (Wuyts et al. 2008) imaging data, calculated with a new algorithm called EAZY. EAZY performs linear combinations of SED templates to find the best fits to measured photometry, which in these two cases span the optical (*UBVRI*) and the IR (*JHK*), as well as the four IRAC bands. They provide values for the $Q_z$ statistic, which indicates the confidence level associated with the inferred redshifts. As explained therein, redshifts with $Q_z < 3$ result in a statistical error of $\sigma_z \equiv \Delta z/(1+z) < 0.1$. Whenever the $Q_z$ statistic is available, we select redshifts using this cut. The MUSYC catalog covers an area of 900 arcmin$^2$ and contains ∼ 17,000 sources, while FIREWORKS extends over a 140 arcmin$^2$ area and has ∼ 6300 sources. The typical redshift errors are $\sigma_z \lesssim 0.04$.

The GOODS-MUSIC (Grazian et al. 2006) catalog contains ∼ 15,000 sources in a region overlapping FIREWORKS. About 6.5% of the redshifts listed in the catalog are spectroscopic, and the others are photometric estimates. The photometric redshifts are based on data at similar wavelengths to those used by Brammer et al. (2008), but the algorithm itself differs from EAZY. Taylor et al. (2009) show that the two sets of redshift estimates are in equally good agreement with the available spectroscopic redshifts. However, this agreement does not suggest which methodology is more accurate for the optically dim, high-redshift sources which dominate in the submillimeter, and for which spectroscopic redshifts are much rarer. The overall photometric redshift error is estimated to be $\sigma_z \sim 0.06$ for both catalogs.

COMBO-17 photometric redshifts (Wolf et al. 2004, 2009) are available for the same region of the sky as MUSYC. The 5 broad and 12 narrow photometry bands from 350 to 930 nm enable accurate SED measurements, although the lack of near infrared data limits COMBO-17 capabilities to estimate redshifts reliably at $z \gtrsim 1.2$. The accuracy of these redshifts is $\sigma_z \sim 0.01$ for galaxies with $R < 21$, 0.02 for galaxies with $R \sim 22$, and 0.1 for those with $R > 24$, which is the sensitivity limit of the survey. Therefore, following other authors (e.g., Le Floc'h et al. 2005), we only use COMBO-17 for sources with listed $R$ magnitude brighter than 24.

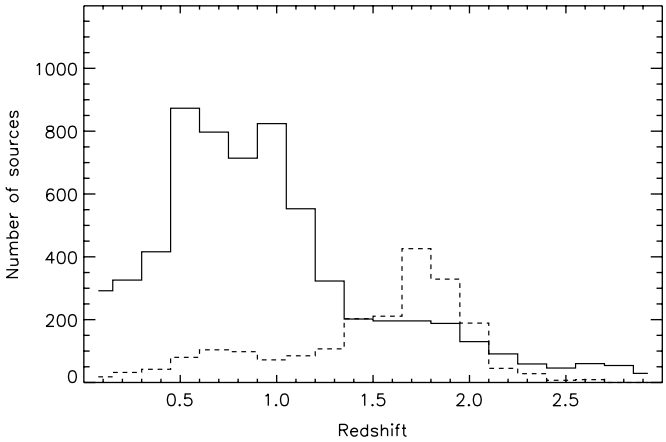


**Figure 2.** Redshift distribution of MIR sources is shown as a solid line for entries having a reliable photometric redshift assigned to them. The distribution peaks between $0.5 < z < 1$ and exhibits a substantial tail up to $z \sim 2$. The dashed histogram shows the distribution of sources with redshifts derived from the IRAC flux density ratios, which tend to cluster at $z \gtrsim 1$.

Finally, Rowan-Robinson et al. (2008) provide a catalog of photometric redshifts for the 24 $\mu$m sources detected in SWIRE over a larger 4.56 deg$^2$ region within BGS-Wide, but with a shallower depth compared to FIDEL. The optical data ($g'\,r'\,i'$) are combined with the two shorter IRAC wavelengths, and are used to fit SED templates. The accuracy in $\sigma_z$ is reported to be 0.035 and is comparable with the above catalogs.

## 3. REDSHIFTS OF MIPS SOURCES

The 9110 sources in the FIDEL catalog have positional accuracies that are significantly smaller than the MIPS PSF (Point Spread Function) at 24 $\mu$m. This is because the catalog positions are obtained from the more accurate near infrared (NIR) IRAC catalog. By matching the FIDEL and redshift catalogs, we identified redshifts for ∼ 72% of the FIDEL sources. We used a search radius of 1″, but using 1.″5 or 2″ does not substantially change the number of identified sources. Given the surface densities of sources in the catalogs (MUSYC has one source every 190 arcsec$^2$, and MUSIC about one every 30 arcsec$^2$), we expect only a few spurious associations within this search radius.

We identified redshifts from the catalogs in the following sequence: (1) FIREWORKS (18%); (2) MUSYC (43%); (3) MUSIC (1%); (4) COMBO-17 (10%); and (5) the catalog of Rowan-Robinson et al. (2008; 0.5%). The redshift distribution (solid line in Figure 2) peaks at $z \sim 0.8$ and shows a high-redshift tail that is particularly significant in the range $1.5 \lesssim z \lesssim 2$.

To determine redshifts for the remaining 28% of the MIR sources with no direct counterparts in the catalogs, we used a relation between IRAC colors and redshifts similar to that derived in Devlin et al. (2009). Redshifts from FIREWORKS and MUSYC were matched to IRAC sources in the SIMPLE catalog. The resulting ∼18,000 objects were binned in a look-up table (LUT) as a function of IRAC flux density ratios. The table is shown in Figure 3 and exhibits a trend of increasing redshift from top-left through top-right to bottom-right. Redshifts for

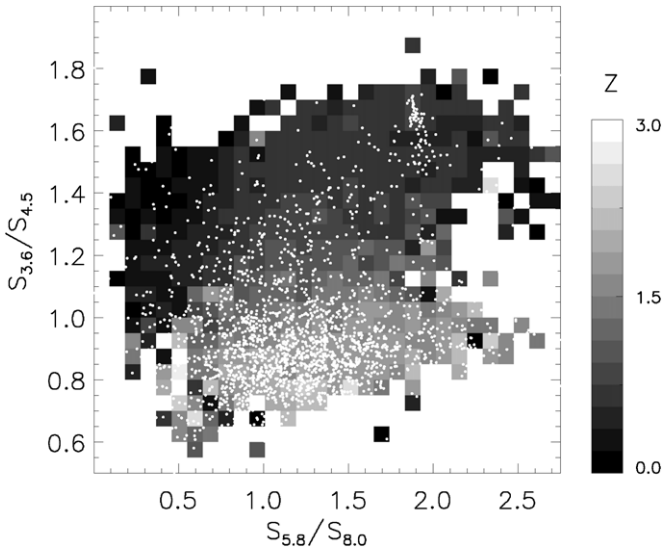


**Figure 3.** IRAC color–color plot of SIMPLE sources with redshifts. Pixels are gray-shaded according to redshift with lighter shades corresponding to higher redshifts. Overplotted as white dots are MIR galaxies in the FIDEL catalog for which no redshift information is available. These points cluster in the bottom region of the plane, suggesting that they may be a population of higher redshift sources. Redshifts were estimated for these objects directly from the means of sources with known redshifts that landed in the same bins of this color–color plane.

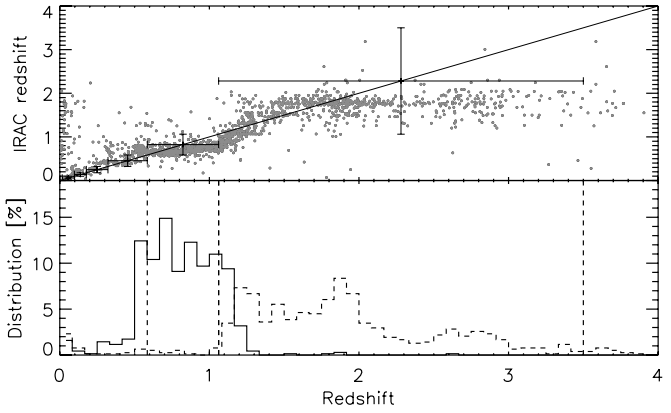


**Figure 4.** Robustness of IRAC redshifts derived from the NIR flux density ratios. The top panel compares the IRAC redshifts with the catalog of photometric redshifts. Although the relation is not linear, its monotonic trend can be used to assign sources to redshift bins, provided these are larger than the scatter introduced. The redshift binning grid is also shown with the crosses indicating the extension of each bin. The distribution of redshifts for sources whose redshift lies in the last two bins is shown in the bottom panel. The in-bin fraction is 68% and 90%.

galaxies are assigned based on the mean values of sources that land in the same bin of the IRAC color–color plane with known redshifts.

A comparison between LUT-retrieved and known redshifts for a number of sources, which have not been used to compile the table, is shown in Figure 4. Although the trend has systematic deviations, as well as a large scatter, the plot exhibits monotonic behavior, and a reliable separation between low and high redshifts. Two plateaus are evident, one at $0.6 < z < 1.1$ and the other at $z > 1.6$.

We initially chose nine redshift bins spanning $0.016 < z < 3.5$ at logarithmically spaced intervals. The first three bins are narrower than the accuracy quoted for the redshift catalogs, so we merged them to form a single bin 4% wide in $\Delta z/(1+z)$. We also merged the last two bins due to the small numbers of sources that landed within them. The six final bins are overplotted in the top panel of Figure 4. The redshift distributions for the sources selected in the last two bins from the IRAC LUT are also shown. Their widths are 68% and 90%, respectively. IRAC redshifts are not reliable in the lower redshift bins.

Almost all of the 28% of the FIDEL sources with no redshifts have flux density ratios populating the bottom region of the IRAC plane, and their IRAC photometric redshift distribution (Figure 2) indicates that they lie preferentially at $z > 0.5$. This is also confirmed by studying the distribution of COMBO-17 redshifts for these sources. Although unreliable in detail, as they are mostly $R \gtrsim 24$, the distribution peaks in the same redshift range.

In summary, we have obtained or estimated redshifts for 95% of the sources from the original MIPS catalog.

## 4. COMPLETENESS

The completeness of the flux-limited FIDEL catalog is investigated in Devlin et al. (2009), finding it to be 63%, 80%, and 96% complete at 20, 40, and 80 $\mu$Jy, respectively. Ideally, one would like to have a similar completeness analysis for each redshift bin used here. Although it is tempting to apply the same corrections, in practice one should consider that the catalog is based on IRAC positions and it would be arbitrary to assume a one-to-one relation between sources missing in FIDEL and sources missing in the underlying SIMPLE catalog. In this work, we have therefore ignored any completeness correction. However, we do indicate what the expected effect might be in the analysis and discussions that follow.

## 5. STACKING ANALYSIS

Stacking analysis using positional information of sources selected at different wavelengths is a powerful tool for estimating the contribution from a given class of objects to the CIB at different wavelengths. In this paper, we have considered the contribution of MIR-selected sources to the CIB as a function of redshift at BLAST and *Spitzer*-70 $\mu$m wavelengths. Our analysis follows the method of Dole et al. (2006). BLAST maps are whitened to suppress the larger scales not relevant to a point-source analysis. The filter, which makes the noise white, is estimated from the smoothed two-dimensional power spectrum of the map. Scales below $\sim 20'$ are also suppressed. The whitening filter gain is taken into consideration when flux densities are measured. The region considered conservatively excludes the edges of the FIDEL and MUSYC area coverage. This region is described by a quadrilateral with corners at the following coordinates (J2000): $3^h31^m36^s$, $-28°02'16''$; $3^h31^m29^s$, $-27°38'34''$; $3^h33^m16^s$, $-27°35'00''$; $3^h33^m26^s$, $-27°58'50''$. A total of 7280 FIDEL sources are in this region, compared to the total 9110 listed in the full catalog.

The means of each map in the stacking region are subtracted, as required by the stacking formulation. We then compile a list of postage-stamp maps centered at the position of each MIR source. These sub-maps are co-added and the total flux density evaluated using aperture photometry. Removing the mean locally before stacking is formally correct; we verified that the standard technique of subtracting the sky estimated in an annulus around the aperture gives a compatible result. Whitening the maps removes all significant large-scale structure so that the postage-stamp maps can be co-added without applying random rotations, as in Dole et al. (2006). Although the

**Table 1**
Stacked Intensities

| λ ($\mu$m) | Total (All Sources) | Total[a] (Sources with Redshift) | Total[b] (Sources with IRAC-$z$ Excluded) | CIB[c] |
|---|---|---|---|---|
| | | $\nu I_\nu$ (nW m$^{-2}$ sr$^{-1}$) | | |
| 70 | $5.4 \pm 0.3$ | $5.2 \pm 0.3$ | $4.6 \pm 0.3$ | ... |
| 250 | $8.2 \pm 0.5$ | $8.1 \pm 0.5$ | $6.1 \pm 0.5$ | $10.4 \pm 2.3$ |
| 350 | $4.8 \pm 0.3$ | $4.8 \pm 0.3$ | $3.3 \pm 0.2$ | $5.4 \pm 1.6$ |
| 500 | $2.0 \pm 0.2$ | $2.0 \pm 0.2$ | $1.2 \pm 0.1$ | $2.4 \pm 0.6$ |

**Notes.** Stacked intensities have not been corrected for completeness, and the quoted errors do not include calibration uncertainties. See Marsden et al. (2009) for the completeness-corrected values.
[a] Stacked intensity from every source with a redshift.
[b] Stacked intensity from every source with a redshift, excluding IRAC-estimated redshifts (see the text in Section 3).
[c] FIRAS-measured background (Fixsen et al. 1998).

SWIRE 70 $\mu$m map was not whitened, the filtering applied by the *Spitzer* reduction pipeline is strong enough to remove large-scale fluctuations. We verified that the retrieved flux densities are the same both by stacking postage-stamp maps directly, and by alternately rotating them by 90° as in the analysis of Dole et al. (2006).

The total retrieved flux density can be overestimated if the distribution of MIR sources is clustered. Marsden et al. (2009) find this effect to be negligible for these catalogs and beam sizes, and it is ignored in the subsequent analysis.

In order to validate the technique and to verify that the analysis pipeline does not introduce artifacts, stacking was performed on noiseless Monte Carlo simulations. Sky realizations were generated at 250 $\mu$m from model counts (Lagache et al. 2003). Source flux densities were drawn from the model and redshifts were assigned from a uniform distribution spanning $0 < z < 2$. Observed 24 $\mu$m flux densities were assigned to each galaxy using Arp 220 as a template to scale from the 250 $\mu$m flux densities given the redshifts. Only 24 $\mu$m flux densities brighter that 13 $\mu$Jy were retained in this list.

We simulated time-stream detector data by scanning the sky realizations with the actual BLAST telescope pointing solution. We then used the BLAST data reduction pipeline, identical to that for the real data, to generate maps.

Stacking was performed on the simulated sky realizations and on the maps obtained from the pipeline, and then compared to the total 250 $\mu$m flux density of the sources in the 24 $\mu$m mock catalog. The three measurements were found to agree within 2%, which is well within the errors.

A final test was carried out by stacking the FIDEL sources on the 24 $\mu$m *Spitzer* map itself. Again, we found that the retrieved flux density was in good agreement with the total flux density in the list.

The uncertainties are estimated as in Marsden et al. (2009) and a similar check for Gaussianity was performed. We also verified that stacking against a catalog of randomly selected positions results in a value of zero.

Our stacking region covers an area of only 590 arcmin$^2$. Sampling variance can thus play an important role, with Dole et al. (2006) suggesting that it can be as large as a factor of 2 (peak to peak). Although we do not presently have comparable data in a different field with which to test this hypothesis, we make a rough estimate by dividing the present field into four separate pieces of roughly equal areas. Stacking in each of these regions independently, we find an rms dispersion of $\sim$ 15% in the retrieved flux densities, which is fairly correlated among the different BLAST and *Spitzer* wave bands. Because of the four sub-fields, the final rms variation is expected to be a factor of 2 smaller than this, although we do not explicitly use this estimate in the error bars later in our analysis. This is probably only a lower limit on the sampling variance as this calculation cannot account for scales larger than 1/4 of the map.

Table 1 lists the results of this analysis. The 70 $\mu$m retrieved intensity is compatible with values from Dole et al. (2006) and Dye et al. (2007). At the BLAST wavelengths these values are within 6% of the ones reported by Devlin et al. (2009), and within 4% of those in Marsden et al. (2009).

The stacked intensities for the 5% of sources with no redshift information is negligible compared to the total ($< 3\%$). The table also lists flux densities retrieved using only sources with redshifts obtained directly from the catalogs (i.e., leaving out the IRAC redshifts). These flux densities are 10%, 30%, 30%, and 40% lower at wavelengths 70, 250, 350, and 500 $\mu$m, respectively. This is broadly expected if the excluded sources lie at high redshift, such that the longer wavelengths are more seriously affected. It also provides a consistency check for the IRAC redshift method discussed earlier.

Although the stacked flux density as a function of wavelength is compatible with the FIRAS detection, given its large error and the sampling variance, it is still possible that a missing population of faint 24 $\mu$m sources is needed to resolve the CIB completely. This is mentioned in Marsden et al. (2009), and we discuss it further in later sections. In any case, it is worth noting that existing estimates of the total resolved CIB are highly uncertain, with FIRAS measurements being affected by systematics and having a formal error of 25%.

## 6. CIB REDSHIFT DISTRIBUTION

The observed CIB is the total dust reprocessed starlight produced in galaxies at all redshifts and luminosities. Splitting the FIDEL catalog into redshifts bins is an effective way to study the contribution that each sub-catalog has to the total intensity. The redshift bins used (see Section 3) were chosen to be at least $\sigma_z$ or larger in $\Delta z/(1+z)$, and the width of the last two bins ensures that the errors in the IRAC redshifts do not result in sources being placed in the wrong bin (Figure 4). The mean stacked intensity in each bin is listed in Table 2.

The cumulative distribution of stacked intensities is shown in Figure 5 as a function of both 24 $\mu$m flux density and redshift, and it is normalized to the total intensity listed in Table 1. We prefer to show this normalization rather than normalizing to the FIRAS measurements because: (1) there is no 70 $\mu$m FIRAS detection and the most accurate detections of the CIB at this wavelength are lower limits; (2) the FIRAS detections in the BLAST bands have large uncertainties; and (3) the BLAST survey is affected by sampling variance, making it difficult to compare with an all sky survey.

A similar qualitative behavior is seen in both the panels of Figure 5, with the stacking measurements at shorter wavelengths dominating the brighter 24 $\mu$m flux densities and the lower redshifts. By redshift 1.1, about 75% of the CIB is generated at 70 $\mu$m, 55% at 250 $\mu$m, 45% at 350 $\mu$m, and 40% at 500 $\mu$m. Similar results are found by Marsden et al. (2009) who estimate these fractions to be 50%, 45%, and 40% at 250, 350, and 500 $\mu$m, respectively (although $z = 1.2$ is the dividing redshift in their study). The relatively small discrepancy at 250 $\mu$m can be accounted for by the different way redshifts are assigned. In this work, most redshifts have been retrieved from catalogs,

**Table 2**
Stacking Analysis Results

| $z_{lo}$ | $z_{hi}$ | $\nu I_\nu$ (70 $\mu$m) | $\nu I_\nu$ (250 $\mu$m) | $\nu I_\nu$ (350 $\mu$m) | $\nu I_\nu$ (500 $\mu$m) | $L_{IR}$[a] | Temperature[a] | Dust Mass[a] | $L_{IR}$ Density | Sources |
|---|---|---|---|---|---|---|---|---|---|---|
| | | (nW m$^{-2}$ sr$^{-1}$) | | | | ($10^9 L_\odot$) | (K) | ($10^7 M_\odot$) | ($10^8 L_\odot$ Mpc$^{-3}$) | in Bin |
| 0.016 | 0.098 | $0.53 \pm 0.04$ | $0.31 \pm 0.07$ | $0.11 \pm 0.04$ | $0.05 \pm 0.02$ | $1.2^{+0.1}_{-0.1}$ | $23.2^{+1.6}_{-0.6}$ [$21.7^{+1.4}_{-1.1}$] | $1.8^{+2.2}_{-1.2}$ [$2.3^{+2.9}_{1.4-}$] | $1.19^{+0.14}_{-0.09}$ | 115 |
| 0.098 | 0.177 | $0.49 \pm 0.04$ | $0.36 \pm 0.08$ | $0.13 \pm 0.04$ | $0.06 \pm 0.03$ | $5.3^{+0.4}_{-0.5}$ | $24.2^{+0.9}_{-1.5}$ [$20.3^{+2.7}_{-0.2}$] | $8.4^{+10}_{-5.1}$ [$11.6^{+15.2}_{-6.9}$] | $1.69^{+0.23}_{-0.13}$ | 169 |
| 0.177 | 0.322 | $0.54 \pm 0.06$ | $0.20 \pm 0.11$ | $0.13 \pm 0.06$ | $0.06 \pm 0.03$ | $9.7^{+1.8}_{-1.2}$ | $29.5^{+1.0}_{-3.3}$ [$26.2^{+3.6}_{-2.1}$] | $7.0^{+9.4}_{-2.8}$ [$9.4^{+13.0}_{-3.0}$] | $1.11^{+0.21}_{-0.15}$ | 323 |
| 0.322 | 0.585 | $1.31 \pm 0.11$ | $1.19 \pm 0.19$ | $0.45 \pm 0.10$ | $0.19 \pm 0.06$ | $41.3^{+3.1}_{-2.7}$ | $29.8^{+1.8}_{-0.2}$ [$26.7^{+0.9}_{-1.9}$] | $32.9^{+38.8}_{-21.9}$ [$49.2^{+61}_{-30}$] | $2.96^{+0.39}_{-0.13}$ | 949 |
| 0.585 | 1.062 | $1.26 \pm 0.16$ | $2.53 \pm 0.30$ | $1.38 \pm 0.16$ | $0.42 \pm 0.09$ | $103^{+10}_{-8}$ | $30.0^{+0.7}_{-2.1}$ [$24.3^{+2.3}_{-0.4}$] | $128^{+154}_{-80}$ [$236^{+297}_{-156}$] | $4.54^{+0.50}_{-0.42}$ | 2247 |
| 1.062 | 3.500 | $1.06 \pm 0.19$ | $3.45 \pm 0.35$ | $2.51 \pm 0.18$ | $1.22 \pm 0.11$ | $899^{+91}_{-98}$ | $36.4^{+4.0}_{-1.7}$ [$34.1^{+1.7}_{-1.4}$] | $936^{+1238}_{-393}$ [$1363^{+1670}_{-758}$] | $6.39^{+0.81}_{-0.53}$ | 3115 |

**Notes.** FIR luminosities, temperatures, and dust masses are the mean values per source in each redshift interval. The FIR luminosity densities are calculated from the mean FIR luminosities as described in Section 8.

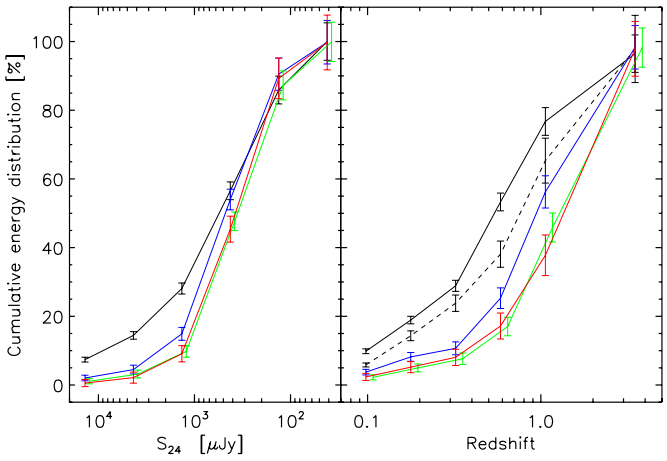


**Figure 5.** Cumulative energy distribution is shown as a function of 24 $\mu$m flux density (left panel) and redshift (right panel) for *Spitzer* at 70 $\mu$m, in solid black, and BLAST in blue (250 $\mu$m), green (350 $\mu$m), and red (500 $\mu$m). The 350 $\mu$m data are shifted by 10% to the right in each panel for visual clarity. Each curve shows the integrated stacked intensity normalized to the total stacked intensity at each wavelength as listed in Table 1. Each data point is plotted in correspondence of the rightmost edge of each bin. Different wavelengths contribute different amounts to the CIB at different epochs, or at different 24 $\mu$m flux densities, with most of the 70 $\mu$m background being generated at $z \lesssim 1$ and the 500 $\mu$m background at higher redshifts. The cumulative plot as a function of flux density shows a similar trend at all wavelengths, suggesting that brighter 24 $\mu$m sources are likely to be at lower redshifts. The cumulative energy distribution for *Spitzer* at 24 $\mu$m is also shown for reference (dashed line in the right panel).

while Marsden et al. (2009) only uses an approximate statistical division into two redshift bins using IRAC colors.

Wang et al. (2006) stacked *H* band and IRAC selected sources in the 850 $\mu$m map of the GOODS-N field. They find that about 70% of the total retrieved flux originates at redshifts $z < 1.5$. This is about 30% of the FIRAS measurement, suggesting that a large fraction of the CIB at this wavelength may be generated at higher redshifts. Serjeant et al. (2008) reach similar conclusions stacking MIR and NIR selected sources.

It is worth mentioning that the fractions of the resolved background depend on the normalization adopted. If FIRAS is used instead, all of these fractions change by as much as 20% at the BLAST wavelengths (not accounting for the quoted measurement uncertainties).

Compared to 70 $\mu$m, the 500 $\mu$m cumulative distribution shows no evidence of convergence in the highest redshift bin, suggesting that a population of faint 24 $\mu$m sources is missing in order to fully resolve the CIB at these longer wavelengths.

## 7. AVERAGE PHYSICAL PARAMETERS

The average flux densities at 70, 250, 350, and 500 $\mu$m from stacking (total stack divided by the number of contributing sources) were used to fit SEDs in each redshift interval to estimate the average FIR luminosities (from 8 to 1000 $\mu$m in the rest frame) of the MIR sources as a function of redshift.

Since the emission mechanism at these wavelengths is thermal, the natural choice of SED is a modified graybody with some emissivity law: $A\,\nu^\beta\,B(\nu, T)$, where $B(\nu, T)$ is the blackbody spectrum and $A$ its amplitude. Such a model assumes a single dust temperature, but the reality is far more complex. Temperature distributions are observed both within single galaxies and among different sources. As a consequence, the resulting spectrum is better described by a power law than a Wien exponential decay at wavelengths shorter than the peak in the SED. Indeed, for our data a modified graybody alone gives a poorer fit to the combined *Spitzer* 70 $\mu$m and BLAST data points, as redshift increases; this is because the 70 $\mu$m channel samples shorter rest-frame wavelengths.

Instead of a blackbody curve modified purely on the Rayleigh Jeans side, we instead used a modified graybody with a fixed emissivity index $\beta = 1.5$, together with a power law decay $\nu^{-\alpha}$ at short wavelengths to prevent the high-frequency SED from falling exponentially. The exponent $\alpha$ is chosen by fitting the SEDs of two often used galaxies: the Ultra Luminous IR Galaxy (ULIRG; $L > 10^{12}\,L_\odot$, $\alpha = 2.8$) Arp 220, and the Luminous IR galaxy (LIRG; $L > 10^{11}\,L_\odot$, $\alpha = 1.8$) M82. The former is a merging system, and the latter is a starburst probably triggered by tidal encounters with the nearby spiral M81. Our fitting procedures estimate the amplitude of the template and the temperature, keeping $\alpha$ and $\beta$ fixed. Both SEDs fit the four data points at each redshift, as shown in Figure 6 for $\alpha = 2.8$; the best-fit quantities are listed in Table 2.

The estimate of FIR luminosity (the integral from 8 to 1000 $\mu$m of the SED in the rest frame) is a weak function of the template (Figure 7), emphasizing that the model need only provide a reasonable interpolation of the data around the peak of the rest-frame FIR emission. The retrieved luminosities increase steeply with redshift. The top panel in Figure 7 plots the mean FIR luminosity as a function of the redshift. It is in good agreement with a similar result found by Le Floc'h et al. (2005), who studied the evolution of FIR luminosities for the same population of 24 $\mu$m sources, although with a higher MIR flux density limit of 80 $\mu$Jy. The figure provides an estimate of the selection effect arising from the flux density limit of the FIDEL catalog, which we assume is 20 $\mu$Jy, the 63% completeness limit. The calculation uses template models for "normal" and "starburst" galaxies from Lagache et al. (2003), co-added after first normalizing to the same FIR luminosity.

As shown in Kennicutt (1998), the FIR emission is tightly correlated with star formation activity (star formation rate, or SFR), under the assumption that star formation is completely optically obscured by dust and that the fraction of infrared

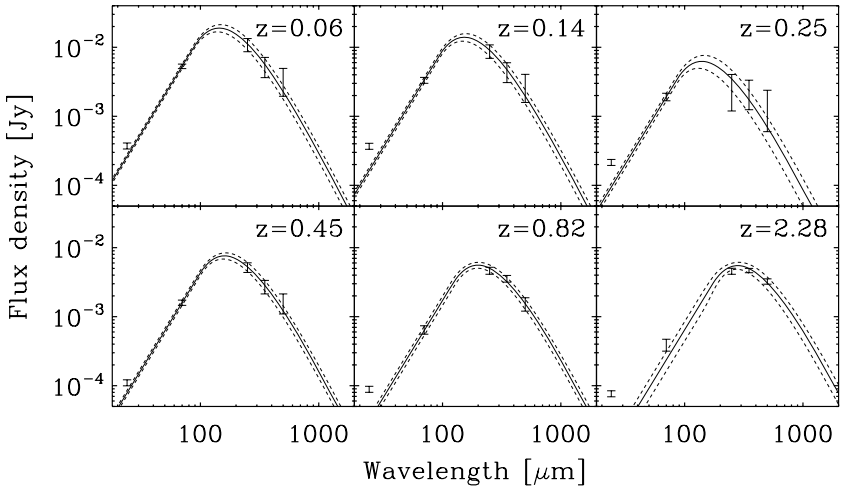


**Figure 6.** SED fitting of the average flux densities measured in different redshift bins. The points with error bars are from BLAST (color-corrected 250, 350, and 500 $\mu$m), and *Spitzer* 70$\mu$m. The solid lines are the best fits at each redshift, with the 68% confidence levels indicated by the dashed lines. The fit accounts for the finite BLAST bandwidths and for the correlated calibration uncertainties. The model template is a modified graybody with an emissivity law $\beta = 1.5$ and a power law $\nu^{-\alpha}$ replacing the Wien part of the spectrum. Two templates were used: one with $\alpha = 2.8$, describing Arp 220's spectrum, and one with $\alpha = 1.8$ that is better matched to M82. Both models are compatible with the data, although for clarity only the $\alpha = 2.8$ fit is shown here. The 24 $\mu$m average flux densities of the sources in the catalog are also shown in each panel for completeness, but are not used in the fits because these fluxes come from regions which are not in thermal equilibrium.

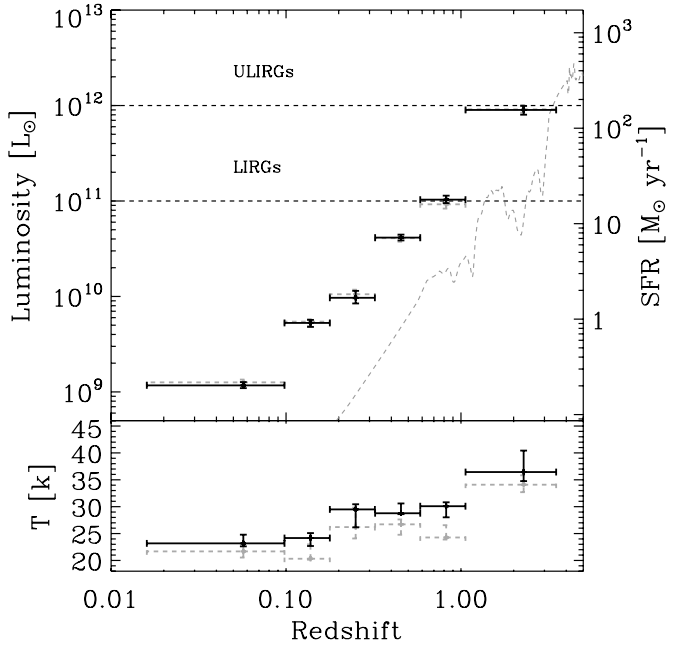


**Figure 7.** Mean rest-frame luminosities, and temperatures of the MIR FIDEL sources are plotted against redshift. In the top panel, the mean FIR luminosities are estimated from the $\alpha = 2.8$ (black points) and $\alpha = 1.8$ (gray, dashed points) SED fits. There is little difference between the two, confirming that the estimated luminosities are a weak function of the template used. The gray dashed line provides an estimate of selection arising from a 24 $\mu$m flux density limit of 20 $\mu$Jy (63% completeness limit of the catalog). The bottom panel shows rest-frame temperatures for both templates. A difference of $\sim 5$ K is observed between the two, with temperatures apparently increasing with redshift.

luminosity dominated by active galactic nucleus (AGN) heating is negligible.[13] Kennicutt (1998) shows that the relation between FIR luminosity and dust obscured SFR is then:

$$\mathrm{SFR}[M_\odot\,\mathrm{yr}^{-1}] = 1.728 \times 10^{-10}\, L\ [L_\odot].$$

We use this relationship to calibrate the SFR axes of the luminosity plots.

From Figure 7, we observe that at low redshifts ($z \lesssim 0.6$) the MIR population is dominated by moderate IR emitters ($L \lesssim 6 \times 10^{10}\, L_\odot$). As the redshift increases, the volume probed also increases and LIRGs become more common, which is consistent with many spheroids being formed at about this time ($z \sim 1$). This is expected, as SCUBA surveys at 850 $\mu$m have revealed the existence of a large number of ULIRG-type objects, residing at typically higher redshifts with a median of $z \sim 2.5$ (Chapman et al. 2003).

Stacking analyses cannot be used to study individual sources, only their average properties. Therefore, we emphasize once more that the quantities estimated are the average values of the population of MIR sources resolving most, if not all, of the CIB detected by FIRAS. For instance, the last bin in Figure 7 probes a redshift range similar to the SCUBA galaxies. However, the mean luminosity is slightly lower than that typically quoted for SCUBA galaxies, suggesting either that some of the most luminous objects (and potentially most optically obscured) are missing from the bin, or that SCUBA galaxies have luminosities that are above average at those redshifts (which is surely true for the extreme objects that have been studied so far at 850 $\mu$m).

Our template fitting returns rest-frame temperatures, but these are more model-dependent than the luminosities. As shown in Figure 7, the difference in the temperatures determined for the two templates is about 5 K across the whole redshift range.

We observe an increase in mean temperature with increasing redshift. This trend can be explained by the correlation observed between temperature and luminosity as discussed by Dunne et al. (2000). Detailed modeling beyond the scope of this paper would be required to determine whether selection or cosmic evolution also play a role.

The average mass in dust can be estimated from the observed flux densities (Hildebrand 1983), $S_\nu(\nu_0)$:

$$M_\mathrm{d} = \frac{D_\mathrm{L}^2(z)}{1+z}\,\frac{S_\nu(\nu_0)}{\kappa\,(\nu_\mathrm{em})\,B_\nu\,(\nu_\mathrm{em}, T)},$$

[13] Devlin et al. (2009) show that the AGN contribution to the CIB at BLAST wavelengths is about 7%, and it is small enough to be ignored.

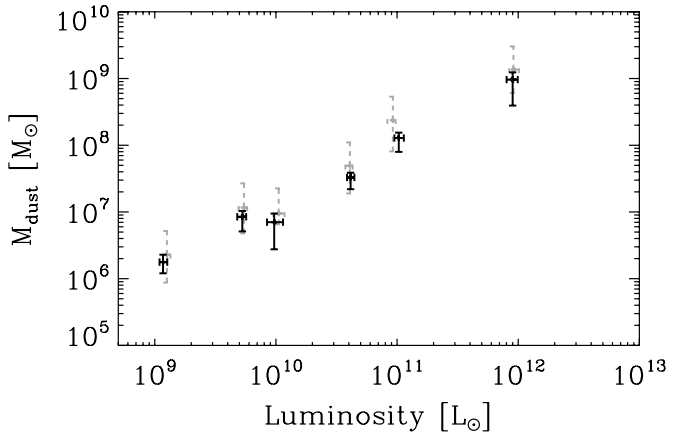


**Figure 8.** Mean dust masses of the MIR FIDEL sources are plotted against the mean FIR luminosities of Figure 7. These masses are calculated using the temperatures estimated from the $\alpha = 2.8$ (black points), and $\alpha = 1.8$ (gray, dashed points) SED fits. Redshifts are not indicated explicitly, but increase monotonically from left to right.

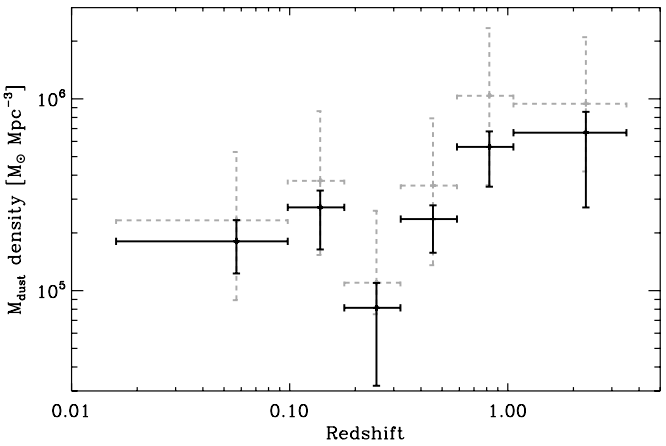


**Figure 9.** Comoving dust mass density vs. redshift. There is only moderate evidence of evolution with redshift.

where $D_L$ is the luminosity distance. The mass-absorption coefficient, $\kappa$, is evaluated at 1 mm ($\kappa_{1\mathrm{mm}} = 0.1\ \mathrm{m^2\ kg^{-1}}$, Hughes 1996), and has a $\nu^\beta$ dependence. Any dust mass estimate has to be treated with caution because: (1) $\kappa_{1\,\mathrm{mm}}$ is uncertain within an order of magnitude (Blain et al. 2002); and (2) the temperature is largely uncertain, and model dependent. We use the flux density at a rest-frame wavelength of 500 $\mu$m, and temperatures obtained from the two model SED fits. The average dust masses are plotted against the average luminosity in Figure 8. Given the monotonic relation between FIR luminosities and redshifts, the leftmost and rightmost points in the figure are the lowest and highest redshift bins, respectively. The dust mass shows a steady increase over 2 orders of magnitude across the probed range of redshifts, and FIR luminosities.

We observe that the estimates of temperature and dust mass from the fit with the $\alpha = 1.8$ template (M82) have larger errors compared to those obtained from the $\alpha = 2.8$ template (Arp 220). This is due to the flatter spectrum close to the emission peak of the $\alpha = 1.8$ template.

## 8. LUMINOSITY AND STAR FORMATION HISTORIES

Mean rest-frame FIR luminosities and dust masses can be converted into comoving-volume densities. The conversion factor applied to each redshift bin is the ratio of the number of sources in the bin to the comoving-volume probed by the bin, which, for a Euclidean geometry, we calculate as

$$V_{\mathrm{com}}(\bar{z}) = \frac{\Omega_{\mathrm{stack}}}{3}\left[\frac{D_L^3(z_{\mathrm{hi}})}{(1+z_{\mathrm{hi}})^3} - \frac{D_L^3(z_{\mathrm{lo}})}{(1+z_{\mathrm{lo}})^3}\right].$$

Here, $\Omega_{\mathrm{stack}}$ is the solid angle of the stacking region, $z_{\mathrm{lo}}$ and $z_{\mathrm{hi}}$ are the edges of each redshift interval, and $\bar{z}$ is the bin center.

Interestingly, the comoving dust mass densities plotted in Figure 9 show little variation over the redshifts probed. This suggests that the amount of comoving dust associated with the FIDEL sources is fairly constant as galaxies are built up. Dunne et al. (2003) found that there was much more dust at $z \gtrsim 1$, although their survey is only sensitive to galaxies with very large dust masses, whereas our stacking analysis is sensitive to galaxies with a wider range of dust masses.

The comoving FIR luminosity densities are shown in Figure 10 and are listed in Table 2. The left vertical axis is converted into SFR density. We used the template with $\alpha = 2.8$ to calculate the luminosities. Also shown is the effect of excluding sources for which redshifts were obtained from the IRAC color–color plane. This potential incompleteness mostly affects the higher redshift bin. We note once again that the error bars include only the statistical uncertainties arising from the stacking and calibration and do not include the effect of sampling variance or incompleteness. This plot is a complete representation of the energetics in the CIB generated by MIR sources at the FIDEL flux density limit, as 95% of these galaxies have been included and the remaining 5% do not contribute substantially to the background.

The luminosity density plot shows the luminosity integrated over the comoving volume. A naïve model is overplotted (not fitted) and is derived from the Saunders et al. (1990) luminosity function (LF) form for *IRAS* galaxies,

$$\Phi_{\mathrm{IR}}(L) = \phi^*_{\mathrm{IR}}\left(\frac{L}{L^*_{\mathrm{IR}}}\right)^{1-\alpha_{\mathrm{IR}}} \exp\left[-\frac{1}{2\sigma^2_{\mathrm{IR}}}\log^2\left(1+\frac{L}{L^*_{\mathrm{IR}}}\right)\right].$$

The coefficients adopted for this model are from Le Floc'h et al. (2005) for a fit to the local FIR LF. The quantity plotted is then

$$\frac{dL}{dV_{\mathrm{com}}} = \int_{L_{\mathrm{min}}}^{\infty} L\ \Phi_{\mathrm{IR}}\left(\frac{L}{f(z)}\right) d\log L.$$

$L_{\mathrm{min}}$ is set to zero in one case (dashed curve) to show the total FIR luminosity density predicted by this model. The solid curve was calculated for $L_{\mathrm{min}}$ estimated assuming a 24 $\mu$m flux density of 20 $\mu$Jy (63% completeness) and our fitting template, and shows the effect of the flux density limit in the FIDEL catalog (higher flux density limits correspond to larger values of $L_{\mathrm{min}}$). The evolution was chosen to be $f(z) = (1+z)^{3.2}$ up to $z = 1.2$, and constant at higher redshifts. This naïve modeling shows good agreement with the data and qualitatively demonstrates the effect of the flux density limit of the catalog. As expected, the only substantial change is to the highest redshift point.

The FIR luminosity densities estimated here show good agreement with similar results obtained from optical detections (Lilly et al. 1996) at $z \lesssim 1$, after a correction for dust extinction has been applied by the authors. Optical measurements are sensitive to the fraction of photons not absorbed by dust. Therefore, dust extinction needs to be taken into consideration in order to estimate the total star formation activity, and to compare with measurements obtained in the FIR. In Figure 10, we also

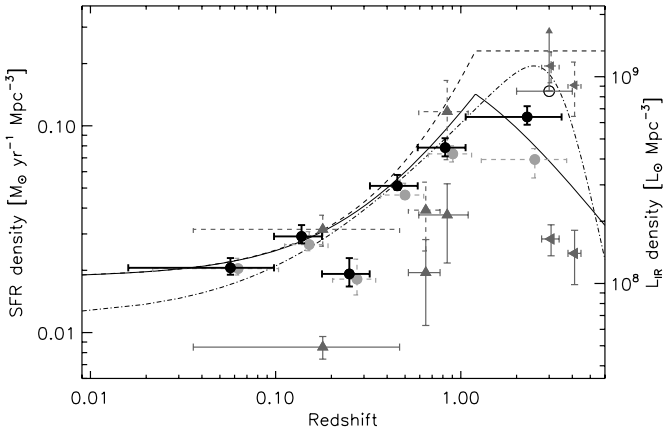


**Figure 10.** Evolution of the total FIR luminosity density up to $z = 3.5$ from MIR-selected sources is shown as black filled circles. The other points are optical–UV detections from Lilly et al. (1996, up-pointing solid triangles) and Steidel et al. (1999, left-pointing solid triangles). These measurements need to be corrected upward for the effects of dust extinction before they can be compared to detections in the FIR, and the corresponding symbols with dashed error bars are the extinction-corrected values. The open circle is the lower limit of Hughes et al. (1998) derived for SCUBA galaxies. SFR is shown on the left axis and shows good agreement with the optical extinction corrected estimates, confirming that most of the star-forming activity in the universe is obscured by dust. The light gray filled circles, with dashed error bars, are calculated from the same MIR population, from which the sources with redshifts estimated from IRAC colors have been removed, and are shifted by 10% toward increasing $z$ for visual clarity. A luminosity function model (not a fit) is plotted as a solid line, and it is also evaluated at a 24 $\mu$m flux density limit of 20 $\mu$Jy to indicate the effect of the FIDEL catalog flux density limit (dashed line). The data also show good agreement with the model of Hopkins & Beacom (2006) (dash-dotted line). The last redshift bin falls lower compared with the SCUBA lower limit (and the extinction-corrected point at similar redshift), and suggests that a fraction of SCUBA galaxies might be a population of faint 24 $\mu$m sources missing from the FIDEL sample.

plot the empirical model of Hopkins & Beacom (2006) obtained from a parametric fit to SFR densities measured at wavelengths spanning from the radio to the UV, which shows good agreement with our measurements.

As the MIR sources resolve most, if not all, of the CIB, at its emission peak, this is the first direct measurement of its energetics and of the dust obscured star formation history of the universe. Although the agreement with previous measurements is remarkably good, previous studies have had to rely on modeling of dust obscuration and SEDs to evaluate FIR luminosities. With the combination of BLAST and *Spitzer*, we have been able to directly probe this quantity with very few assumptions about the underlying physical details.

Comparing our measurements with the optical measurements (the triangle symbols with solid error bars in Figure 10), we find that the fraction of light from young stars hidden by dust is about 70% in the range $0.1 < z < 1$.

The highest redshift bin, which coincides with the redshifts at which SCUBA galaxies are typically found, is the most affected by the FIDEL flux density limit. Comparing with the lower limit on the SFR density for SCUBA galaxies of Hughes et al. (1998), it appears as if some fraction of this population is missing from the FIDEL catalog, which does not contain large fractions of ULIRG-type objects, as discussed in the previous section. It is possible that a significant fraction of SCUBA galaxies have fainter 24 $\mu$m flux densities than the threshold we used for the FIDEL catalog, although we note that many SCUBA sources have had 24 $\mu$m counterparts identified in past surveys (e.g., Pope et al. 2006; Ivison et al. 2007). However, here we are talking about the sources dominating the background at 850 $\mu$m, which are fainter than the typical sources detected by SCUBA. This is indicated by our simple luminosity function model, which suggests that a substantial number of low-luminosity sources are missing from the catalog at high redshifts. It also may be possible that some of the high-redshift sources in our catalog have simply been misidentified as lower redshift objects, but due to their relatively small numbers, have little effect on the lower redshift bins.

Either way, there is evidence that this study misses a portion of the SFR history at the highest redshifts ($z > 1$), during which it is believed the most massive galaxies were forming through powerful mergers. This is consistent with the result of Marsden et al. (2009) who find the contribution of FIDEL sources to the CIB at 850 $\mu$m to be significantly low compared to the FIRAS measurements. They also find that their estimate of the CIB generated at 850 $\mu$m by sources with $z > 1.2$ is low compared to the model of Valiante et al. (2009), which otherwise fits the CIB at the BLAST wavelengths.

## 9. CONCLUSIONS

We have studied the contribution of MIR galaxies selected at 24 $\mu$m to the CIB and found that they resolve most, if not all, of the radiation detected by the all-sky FIRAS and DIRBE surveys at the peak of the far-infrared background. We assigned redshifts to more than 70% of this population from existing redshift catalogs, and developed a technique which uses the NIR IRAC colors to statistically assign redshifts to the remainder of the catalog. Using a stacking analysis to overcome the confusion noise arising from the finite instrumental resolution, we study the composition of the CIB as a function of redshift. We find that 60% of the CIB at 500 $\mu$m is generated at redshifts $z > 1.1$, while the 70 $\mu$m background has a more recent origin, with 75% of it being generated at redshifts $z < 1.1$.

By fitting SEDs to the mean flux densities at each redshift, we have shown that, on average, this population is consistent with being predominantly lower luminosity LIRGs rather than the ULIRGs detected in SCUBA surveys. It appears that a significant fraction of the submillimeter galaxies known to exist at redshifts $z > 2$ are missing from our analysis, and we conjecture that they are simply below the 24 $\mu$m flux density limit in our source catalog, or perhaps in some cases have had their redshifts misidentified. However, while such objects are important at high redshifts, their contribution to the peak of the CIB is small compared with the bulk of the MIR-selected galaxies at lower redshifts.

The evolution in the total comoving FIR luminosity density can be evaluated using MIPS and BLAST data directly, as these wavelengths span the rest-frame FIR peak emission. This evolution can then be directly converted into the SFR history. We find good agreement with existing studies conducted at optical–UV wavelengths, which have had to rely on many more assumptions about physical source properties.

Our results confirm that dust obscuration dominates the history of star formation of the universe, with SFRs that are about three times larger than in the optical–UV, in the redshift range $0.1 < z < 1$.

These results can be used to constrain models of luminosity densities and galaxy formation as they directly probe the FIR energetics of the universe up to redshift $z \sim 3$.

We acknowledge the support of NASA through grant numbers NAG5-12785, NAG5- 13301, and NNGO-6GI11G, the NSF

Office of Polar Programs, the Canadian Space Agency, the Natural Sciences and Engineering Research Council (NSERC) of Canada, and the UK Science and Technology Facilities Council (STFC). This work is based in part on observations made with the *Spitzer Space Telescope*, which is operated by the Jet Propulsion Laboratory, California Institute of Technology under a contract with NASA.

The authors are grateful to Hervé Dole for fruitful suggestions on the analysis, and to Benjamin Magnelli for help with the FIDEL 24 $\mu$m data.

## REFERENCES

Blain, A. W., Smail, I., Ivison, R. J., Kneib, J.-P., & Frayer, D. T. 2002, Phys. Rep., 369, 111
Brammer, G. B., van Dokkum, P. G., & Coppi, P. 2008, ApJ, 686, 1503
Chapman, S. C., Blain, A. W., Ivison, R. J., & Smail, I. R. 2003, Nature, 422, 695
Damen, M., Labbé, I., Franx, M., van Dokkum, P. G., Taylor, E. N., & Gawiser, E. J. 2009, ApJ, 690, 937
Devlin, M. J., et al. 2009, Nature, 458, 737
Dole, H., et al. 2006, A&A, 451, 417
Dunne, L., Eales, S. A., & Edmunds, M. G. 2003, MNRAS, 341, 589
Dunne, L., Eales, S., Edmunds, M., Ivison, R., Alexander, P., & Clements, D. L. 2000, MNRAS, 315, 115
Dwek, E., et al. 1998, ApJ, 508, 106
Dye, S., Eales, S. A., Ashby, M. L. N., Huang, J.-S., Egami, E., Brodwin, M., Lilly, S., & Webb, T. 2007, MNRAS, 375, 725
Dye, S., et al. 2009, ApJ, 703, 285
Fixsen, D. J., Dwek, E., Mather, J. C., Bennett, C. L., & Shafer, R. A. 1998, ApJ, 508, 123
Grazian, A., et al. 2006, A&A, 449, 951
Griffin, M. J., Swinyard, B. M., & Vigroux, L. G. 2003, Proc. SPIE, 4850, 686
Hauser, M. G., & Dwek, E. 2001, ARA&A, 39, 249
Hauser, M. G., et al. 1998, ApJ, 508, 25
Hildebrand, R. H. 1983, QJRAS, 24, 267
Hopkins, A. M., & Beacom, J. F. 2006, ApJ, 651, 142
Hughes, D. H. 1996, in Astrophysics and Space Science Library, Vol. 206, Cold Gas at High Redshift, ed. M. N. Bremer & N. Malcolm (Dordrecht: Kluwer), 311
Hughes, D. H., et al. 1998, Nature, 394, 241
Ivison, R. J., et al. 2007, MNRAS, 380, 199
Kennicutt, R. C., Jr. 1998, ARA&A, 36, 189
Knox, L., Cooray, A., Eisenstein, D., & Haiman, Z. 2001, ApJ, 550, 7
Lagache, G., Dole, H., & Puget, J.-L. 2003, MNRAS, 338, 555
Lagache, G., Puget, J.-L., & Dole, H. 2005, ARA&A, 43, 727
Le Floc'h, E., et al. 2005, ApJ, 632, 169
Lilly, S. J., Le Fevre, O., Hammer, F., & Crampton, D. 1996, ApJ, 460, L1
Lonsdale, C. J., et al. 2003, PASP, 115, 897
Magnelli, B., Elbaz, D., Chary, R. R., Dickinson, M., Le Borgne, D., Frayer, D. T., & Willmer, C. N. A. 2009, A&A, 496, 57
Marsden, G., et al. 2008, Proc. SPIE, 7020, 702002
Marsden, G., et al. 2009, ApJ, 707, 1729
Papovich, C., et al. 2004, ApJS, 154, 70
Pascale, E., et al. 2008, ApJ, 681, 400
Patanchon, G., et al. 2008, ApJ, 681, 708
Patanchon, G., et al. 2009, ApJ, 707, 1750
Pope, A., et al. 2006, MNRAS, 370, 1185
Puget, J.-L., Abergel, A., Bernard, J.-P., Boulanger, F., Burton, W. B., Desert, F.-X., & Hartmann, D. 1996, A&A, 308, L5
Rowan-Robinson, M., et al. 2008, MNRAS, 386, 697
Saunders, W., Rowan-Robinson, M., Lawrence, A., Efstathiou, G., Kaiser, N., Ellis, R. S., & Frenk, C. S. 1990, MNRAS, 242, 318
Serjeant, S., et al. 2008, MNRAS, 386, 1907
Steidel, C. C., Adelberger, K. L., Giavalisco, M., Dickinson, M., & Pettini, M. 1999, ApJ, 519, 1
Taylor, E. N., et al. 2009, ApJS, 183, 295
Truch, M. D. P., et al. 2008, ApJ, 681, 415
Truch, M. D. P., et al. 2009, ApJ, 707, 1723
Valiante, E., Lutz, D., Sturm, E., Genzel, R., & Chapin, E. 2009, ApJ, 701, 1814
Viero, M. P., et al. 2009, ApJ, 707, 1766
Wang, W.-H., Cowie, L. L., & Barger, A. J. 2006, ApJ, 647, 74
Wolf, C., Hildebrandt, H., Taylor, E. N., & Meisenheimer, K. 2009, A&A, 492, 933
Wolf, C., et al. 2004, A&A, 421, 913
Wuyts, S., Labbé, I., Schreiber, N. M. F., Franx, M., Rudnick, G., Brammer, G. B., & van Dokkum, P. G. 2008, ApJ, 689, 653